Journal of Building Engineering 34 (2021) 101901

Contents lists available at ScienceDirect

Journal of Building Engineering

journal homepage: http://www.elsevier.com/locate/jobe

Experimental and numerical analysis of airflow around a building model with an array of domes

Mohammad Mehdi Tavakol [a,*], Mahmood Yaghoubi [b], Goodarz Ahmadi [c]

[a] Department of Mechanical Engineering, Shiraz Branch, Islamic Azad University, Shiraz, Iran
[b] School of Mechanical Engineering, Shiraz University, Shiraz, Iran
[c] Department of Mechanical and Aeronautical Engineering, Clarkson University, NY, USA

ARTICLE INFO

Keywords:
Array of domes
Building
CFD
Hot-film anemometer
LES
Turbulent flow
Wind tunnel

ABSTRACT

Domed and curved structures are widely used in the hot arid regions of Iran and other Middle Eastern countries because of their ventilation advantages. Many experimental and numerical studies were reported for the wind flow over a single dome or single vault. However, studies of the airflow around an array of domes, which are important for designing or constructing these structures, are scarce. In this study, the wind flow around a building model with an array of domes was studied experimentally and numerically. A hot-film anemometer was used, and airflow velocity profiles around the building model in a wind tunnel were measured. The RANS approach and the large eddy simulation (LES) were used, and simulations were performed for Reynolds numbers of 43,000 and 430,000. The predicted streamwise mean velocity and root-mean-square fluctuation velocity profiles around the model were compared with the wind tunnel data, and good agreements were observed. The presented results indicated that the separation points over the domes move further downstream for the second and third domes compared with the first dome. Also, the peak suction pressure was observed over the first dome near the dome apex, and the maximum pressure was seen in the windward side of the third dome. The results were compared with the case of airflow around a single dome, and the influence of the dome's location in the array was discussed. Also, recommendations for the design or construction of buildings with an array of domes were provided.

1. Introduction

Understanding the wind flow around buildings is essential for many engineering applications, including evaluation of aerodynamic forces, pedestrian level wind patterns in urban design, appropriate design of heating, ventilation, and air-conditioning (HVAC) systems, and pollutant dispersion and human exposure. Predicting the airflow velocity and pressure fields around buildings is also essential for their structural design and the design of effective ventilation systems. Such knowledge can be obtained through accurate wind tunnel experiments and, or numerical simulations of turbulent wind flows around buildings of interest.

1.1. Literature review

Several experimental studies for determining the pressure distributions (wind loads) on domes were reported in the past several decades. The early wind tunnel study of Maher [1] was performed for a uniform airflow at low turbulence intensity. Later, Taniguchi et al. [2], Toy et al. [3], Newman et al. [4], and Savory and Toy [5] accounted for the atmospheric turbulent boundary layer and presented their experimental data for various Reynolds numbers. Ogawa et al. [6], Taylor [7], and Letchford and Sarkar [8] reported their experimental results for fluctuating pressures on the surface of domes. Cheng and Fu [9] experimentally investigated mean and fluctuating pressure distributions on a wall-mounted dome for various Reynolds numbers.

Tamura et al. [10] performed a series of numerical simulations to investigate the unsteady wind flow and pressure around a dome-shaped structure. They also reported the structure of flow in the dome near the wake region. Meroney et al. [11] simulated turbulent flows around an isolated dome and an array of two domes and compared the mean pressure distribution on these structures. They also reported the equivalent mean pressure distribution at low $Re = 1.85 \times 10^3$ and high $Re = 1.44 \times 10^6$ and found similar flow separation and reattachment patterns. Fu et al. [12] employed LES and studied the aerodynamic characteristics

* Corresponding author.
E-mail address: tavakolmm@shirazu.ac.ir (M.M. Tavakol).

https://doi.org/10.1016/j.jobe.2020.101901
Received 1 July 2020; Received in revised form 14 October 2020; Accepted 16 October 2020
Available online 21 October 2020

Nomenclature

D	Hemisphere diameter
H_b	Building height
H_{ref}	Reference height
I	Turbulence intensity
k	Turbulence kinetic energy
L	Large scale length
L_{ij}	Leonard stress tensor
p	Mean pressure
Re	Flow Reynolds number
S_{ij}	Resolved strain rate tensor
T_L	Time scale of large eddies
u_i	Resolved velocity components
u_τ	Friction velocity
u*	Friction velocity
U	Reference wind velocity
x_i	Coordinates
y	Wall distance
y_0	Aerodynamic roughness height

Greek letters

δ_{ij}	Kronecker delta
ε_{SGS}	SGS dissipation rate
ρ	density
κ	von Karmman constant
λ_t	Taylor time scale
ν	Kinematic viscosity
τ	Characteristic time scale
τ_{ij}	SGS stress tensor
τ_η	Kolmogorov time scale
Γ_i	Circulation
Δ	Grid filter
Δ	Test filter

of a hemispherical dome in smooth and rough turbulent boundary layer flows at $Re = 2 \times 10^6$. They used experimental data of Cheng and Fu [9] for validation of their numerical simulations. Using the validated LES approach, they studied the location of separation over the dome and the characteristics of flow near the separation point.

Domes and arcs are two important kinds of roofs that have been historically used in hot-arid regions in Iran and other countries in the Middle-East. This is due to the domed roof structural and airflow ventilation advantages. In particular, several authors described the benefits of domed roofs. Bahadori and Haghighat [13] studied the passive cooling of buildings and found that the buildings with the domed roof are more effective than those with flat roofs. Yaghoubi [14] reported that the domed roof restricts the heat exchange between the hot outdoor air and the building envelope and decreases the heat gain in a hot environment due to the larger shadow area compared to the flat roof. Asfour and Gadi [15] simulated wind-induced natural circulation in buildings with a domed roof in terms of airflow rate and internal airflow distribution. They observed improvement for ventilation performance in the building with a domed roof. Faghih and Bahadori [16,17] investigated the pressure distribution over a domed roof experimentally and numerically.

Hadavand and Yaghoubi [18] performed numerical simulations and studied heat transfer from curved roofs for various wind velocities and rim angles. They compared the surface temperature and heat transfer coefficient with those for a flat roof of the same size and orientation. They found a substantial difference between the heat transfer coefficient and heat flow between the vaulted and flat roofs.

Sedighi et al. [19] studied the thermal performance of an array of three consecutive domes by incorporating the influence of solar radiation received by the dome surface and the wind speed and direction. They concluded that the main reason for the thermal comfort in the interior of dome-shaped structures is the formation of the stack effect and air exchange from their top opening rather than by shading characteristics of domes by nearby domes.

Kharoua and Khezzar [20] used the LES and studied turbulent airflow around smooth and rough hemispherical domes. The roughness was introduced over the dome surface using solid blocks extruded with the size of glass beads used in the experimental study of Savory and Toy [21]. They presented the variation of pressure coefficients over the dome and the Reynolds stress distribution at various dome sections near the wake region. While a satisfactory agreement of the LES prediction with the experimental data was found, the Reynolds stress peaks and pressure coefficient for the rough dome were over-predicted. Tavakol et al. [22] used the LES with various SGS models and studied turbulent airflow around a wall-mounted hemisphere at Re = 36,000 and 64,000. Comparisons of the predicted time-averaged velocity profiles at different sections in the symmetry plane with the experimental data revealed that the LES is superior compared to the RANS simulation. Mean surface pressure distribution, as well as streamlines, were also presented and discussed.

Wood et al. [23] undertook a combined numerical and experimental study and evaluated the turbulent flow past a hemispherical obstacle. Their measurements were conducted by the Laser-Doppler and hot-film probes, and the LES was employed for numerical simulations. They reported the time-averaged and fluctuating field in the near wake region of the hemisphere. They also emphasized the importance of approaching turbulence intensity on the size and intensity of the upstream horseshoe vortex and the location of the separation line on the hemisphere surface.

In a recent study, Cao and Tamura [24] conducted an LES study of flows around a wall-mounted hemisphere immersed in a boundary layer flow at $Re = 7 \times 10^4$–7×10^5, covering both subcritical and supercritical flows. Drag and lift forces were examined simultaneously, and the critical Reynolds number (when drag and lift forces exhibit steep variation) of $Re = 3 \times 10^5$ was identified. Their analysis indicated strong Reynolds number dependence and delayed flow separation over the hemisphere with a smaller reversed flow zone behind the obstacle. At the symmetry plane, the system of primary horseshoe vortex and smaller vortices were observed.

Table 1 provides an overview of selected experimental and numerical studies regarding airflow around a wall-mounted hemisphere, a single hemisphere dome, and an array of domes. In this table, DNS stands for the Direct numerical simulation, Exp denote Experiment, LES is the Large-eddy simulation, and RANS is the Reynolds averaged Navier-Stokes, with SRANS being steady RANS.

Also, here, the Reynolds number and the shear Reynolds number are defined, respectively, as $Re = \frac{UD}{\nu}$, $Re_{u_\tau} = \frac{u_\tau D}{\nu}$, where U is the wind velocity, u_τ friction velocity, and D is the hemisphere/dome diameter. Table 1 shows the type of the study (experimental or numerical), range of Reynolds number, and a summary of reported results. This table indicates that most reported studies on flows around domes and domed shape roofs were conducted for a single dome, and studies of multiple domes in an array are scarce.

1.2. Research gaps and objectives

According to the above literature survey, there are only a few reported studies on the aerodynamic behavior of airflow over an array of domes. To the best of authors' knowledge, the aerodynamic performance of dome arrays and aerodynamic interference of domes using SRANS and LES were not reported in the literature. Wind-induced

Table 1
Selected studies of airflow around wall-mounted hemisphere(s)/dome(s).

Ref:	Method	Case	Reported data
Maher [1]	Exp.	Hemisphere 9.2×10^5<Re< 1.84×10^6	Mean pressure measurement
Taniguchi et al. [2]	Exp.	Hemisphere –	Pressure coefficient, drag and lift coefficients
Toy et al. [3]	Exp.	Hemisphere Re = 1.6×10^5	Mean and RMS velocity, Pressure measurement
Newman et al. [4]	Exp.	Rigid and flexible domes with different height Re_{ut} = 11,000	Pressure distribution
Savory and Toy [5]	Exp.	Hemisphere Re = 1.4×10^5	Flow visualization, wake structure, pressure measurement
Savory and Toy [21]	Exp.	Hemisphere, Hemisphere cylinder 1.31×10^4<Re< 1.4×10^5	Flow visualization, wake structure
Suzuki et al. [25]	Exp.	Hemisphere Re = 3×10^5	Pressure fluctuations
Acarlar and Smith [26]	Exp.	Hemisphere 60 < Re < 6400	Flow visualization in a water channel, structure of near wake and far wake
Savory and Toy [27]	Exp.	Hemisphere and hemisphere cylinder Re = 1.4×10^5	Normal and Shear stress distribution in the wake
Tamura et al. [10]	Num. Direct simulation (Pseudo DNS)	Dome Re = 2×10^3, Re = 2×10^4	Mean and fluctuating velocity and pressure filed
Taylor [7]	Exp.	Hemisphere 1.1×10^5<Re< 3.1×10^5	Pressure measurement
Yaghoubi [14]	Exp.	Array of dome –	Flow visualization
Manhart [28]	Num. LES	Hemisphere Re = 1.5×10^5	Mean and fluctuating velocity Vortex shedding process
Letchford and Sarkar [8]	Exp.	Dome Re = 4.6×10^5	Mean and fluctuating pressure
Meroney et al. [11]	Num./SRANS	Single dome, dual domes Re = 4.6×10^5	Mean pressure, drag and lift coefficients
Asfour and Gadi [15]	Num.	Building with domes –	Flow pattern, ventilation rate
Faghih and Bahadori [16, 17]	Exp. Num./SRANS	Domed roof Re = 5.8×10^5	Pressure distribution, heat transfer coefficient
Hadavand and Yaghoubi [18]	Num.	Vaulted roof 5×10^5<Re< 2×10^6	Convection and radiation heat transfer
Cheng and Fu [9]	Exp.	Hemisphere 5.3×10^4<Re< 2×10^6	Mean and fluctuating pressure distribution
Tavakol et al. [29]	Exp, Num./SRANS	Hemisphere Re = 6.4×10^4	Mean and RMS velocity field
Kharoua and Khezzar [20]	Num./LES	Hemisphere Re = 1.4×10^5	Velocity and pressure field
Fedrizzi et al. [30]	Exp.	Hemisphere, 6.36×10^4<Re< 1.55×10^5	Pressure measurement, Visualization
Rahmatmand et al. [31]	Exp./Num. /SRANS	Domed roof Re = 1.22×10^5	Mean and RMS Velocity Ventilation
Fu et al. [12]	Num./LES	Hemisphere Re = 2×10^6	Mean and RMS pressure
Tavakol et al. [22]	Num.LES /RANS	Hemisphere Re = 3.6×10^4, 6.4×10^4	Mean and RMS Velocity Vortical structure
Sedighi et al. [19]	Exp./Num.	Dome–	Solar radiation, heat transfer
Wood et al. [23]	Exp. Num./LES	Hemisphere Re = 5×10^4	Instantaneous flow structure, Vortical structure
Cao and Tamura [24]	Num./LES	Hemisphere 7×10^4<Re< 7×10^5	Instantaneous flow structure, flow structure frequency

airflow fields around isolated buildings produce three-dimensional anisotropic flows with high pressure-gradients, vortical structures, and instabilities due to flow separation from the building's leading-edge and lateral sides. The streamwise vortices generated in the flow affect the wake structure and produce the spanwise gradients, which affect the turbulent mixing process. On the other hand, the velocity and pressure instabilities around the building occur because of the strong velocity gradients around the obstacle. For an array of bluff bodies like domes located in the proximity of each other, the flow is more complex because the disturbance caused by each dome affects the flow structure around the nearby domes. Such interference influences the vortex shedding process and separation and reattachment locations.

In desert areas in Iran and other Middle Eastern countries, old bazaars were usually built with a series of domed roofs [19]. Important advantages of domed roofs are their providing passive cooling in dry and hot climate areas, for which the airflow patterns over the domes play an important role. While the airflow over a single dome has been extensively studied, airflows over roofs with arrays of domes have not been investigated. In particular, the interaction of airflows over one dome with the sequence of domes is not fully understood. Among important conclusions, it was demonstrated that for a single dome, the minimum pressure coefficient occurs at the dome apex [16]. However, for an array of domes, the locations of minimum pressure are not known. The airflow pattern and pressure distribution around the dome arrays also affect the performance of the air conditioning equipment in the new structures, and dispersion and deposition of dust particles suspended in the air.

Fig. 1 shows a sample residential building with domed roof arrays in the city of Shiraz in Fars province of Iran. Fig. 2 shows a picture of the array of domes over the bazaar in the city of Kerman. Many buildings in Kerman have benefited from this kind of roof for passive cooling purposes [16,18,19].

Fig. 1. An array of domes on a rooftop.

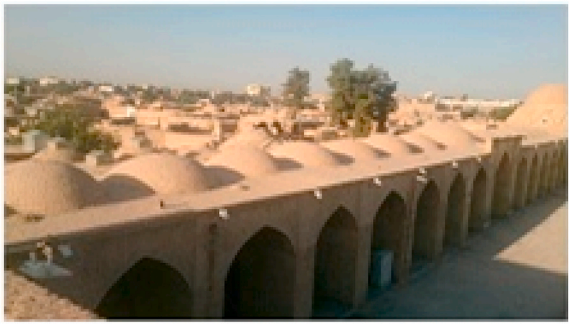

Fig. 2. An array of domes over a building in Kerman, Iran.

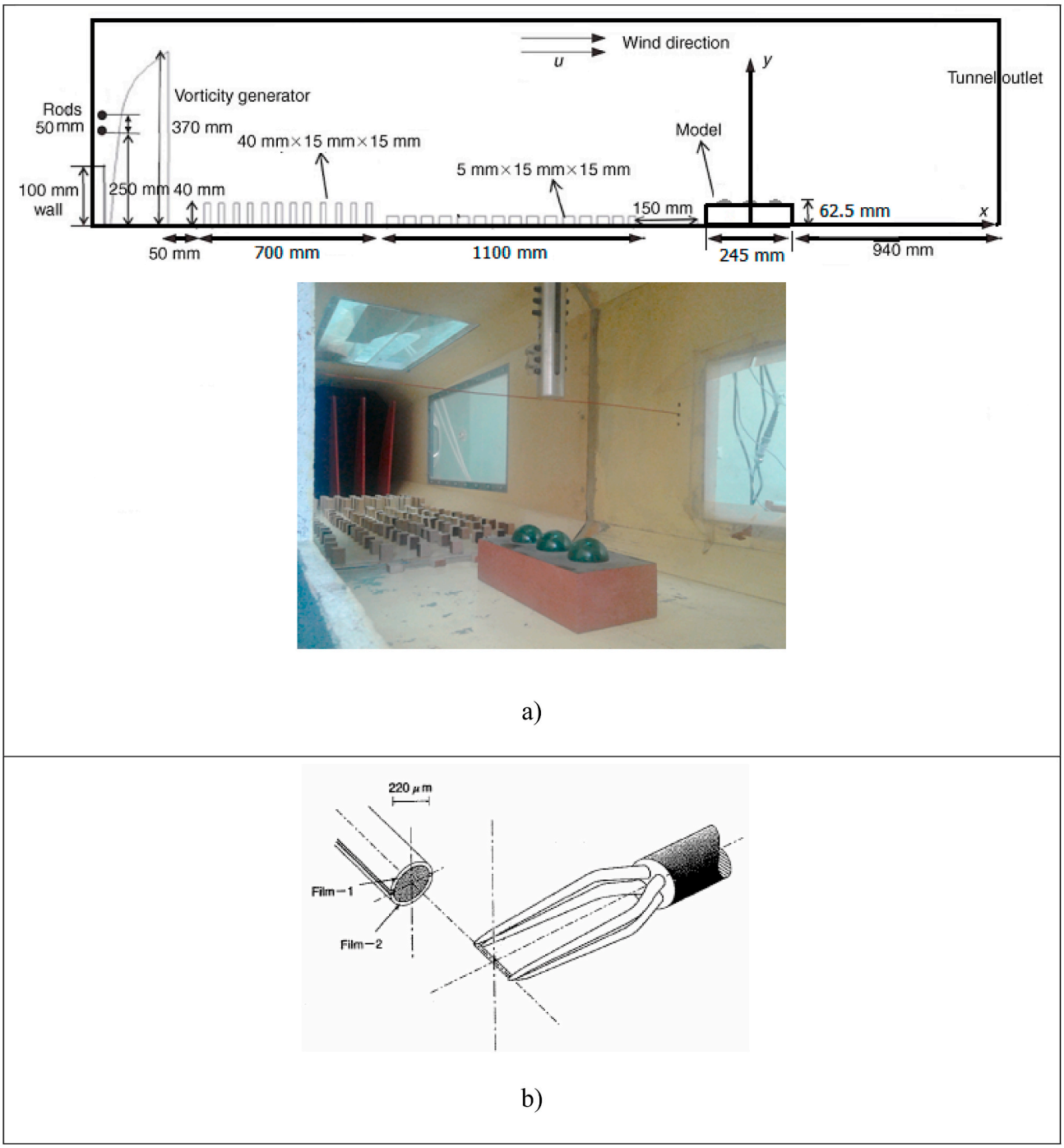

Fig. 3. a) Wind tunnel setup, including an array of domes model, barrier, and vorticity generators, b) Tip of the split fiber sensor.

2. Methodology

In the current study, the turbulent airflows around a building model with three identical domes on their rooftop were evaluated. These domes combination that is shown in Fig. 2 resemble a model of many old bazaars in Iran and other Middle Eastern countries. In a previous study, Tavakol et al. [22] found that the SRANS could not correctly predict the airflow around the domes. However, they showed that the LES with a proper sub-grid scale model could model the boundary layer flow around the hemisphere with reasonable accuracy. Therefore, in the current study, the numerical simulations were performed using the LES approach, and the structure of airflow around the array of domes was examined. The results are compared with those of the RNG k-ε model. The LES results for the streamwise mean velocity and root-mean-square (RMS) fluctuation velocity profiles were also compared with the wind tunnel data, and good agreement was observed. In addition, the influence of grid resolution on the prediction of mean and RMS streamwise velocity around the building model was evaluated and discussed. The aerodynamic performance of domes in an array was compared with the case of a single dome/hemisphere, and recommendations for the design of domed array structures were presented. In section 2.1, the experimental setup and measurement technique is explained, and in section 2.2, details of the numerical model, including the computational domain and boundary conditions, are described. Then, results are presented in section 3.

2.1. Experimental study

The literature survey shows that the flow structure around a single dome in a turbulent boundary layer is quite complicated. Flows around dome arrays, however, are even more complex due to the aerodynamic interference of domes, the formation of multiple separation zones, and unsteady flow characteristics such as vortex shedding. Here, experimental and numerical studies were used to study the flow around dome arrays. First, the wind tunnel was prepared to produce an artificial atmospheric boundary layer for studying the flow around a building model with a dome array roof. The mean and fluctuating velocity components at various locations around the model and near the dome array were measured using a calibrated hot-film probe. For spectral analysis, an instantaneous velocity record in the leeward side of the building model was obtained and used to identify the vortex shedding process around the model. The above time-averaged and instantaneous data provided insight into the flow field around the building model. The collected experimental data were used for the validation of complementary numerical analysis using RANS and LES models.

In the subsequent sections, the experimental facilities, including the wind tunnel, the building model, and the hot film probe, are described. The method for producing the artificial boundary layer flow in the wind tunnel is then presented. The measurement technique using the hot-film probe in the wind tunnel is also discussed in subsection 2.1.2.

2.1.1. Experimental setup

All experiments were carried out in the wind tunnel lab of the School of Mechanical Engineering at Shiraz University. The open-circuit wind tunnel operates as a blowing type. The wind tunnel and the model arrangement in the tunnel are shown in Fig. 3. The tunnel cross-section is 0.46 m wide 0.46 m with a 3.26 m long test section. An AC inverter with variable frequency controls the airspeed in the tunnel up that could reach a maximum of 25 m/s. The atmospheric boundary layer (ABL) profile was generated in the tunnel using a set of barriers and vorticity generators. This method was introduced by Counihan [32] and was used in the earlier studies of Rahmatmand et al. [31] and Tavakol et al. [29].

The tunnel uses quarter-elliptic vortex generators and a castellated barrier wall to produce the initial momentum defect in the boundary layer. They are followed by a fetch of roughness elements that resemble the terrain. The roughness elements consisted of a staggered arrangement of cuboids mounted in two consecutive rows, as shown in Fig. 3. As noted by Cook [33], the building model and the atmospheric boundary layer (ABL) must be scaled by the same factor to properly simulate the influence of wind on the building. The roughness length and the longitudinal integral length scale of streamwise turbulence fluctuations are other important parameters. The former was calculated by fitting the measured mean velocity distribution to the logarithmic velocity profile. In addition, the turbulence intensity is important to represent the realistic ABL in the tunnel, and it should match the full-scale data of ABL (ESDU 1985 [34]).

Following the procedure proposed by Cook [33] and modified by De Bortoli et al. [35] for the part-depth (the lower part) simulation of ABL, the scale factor of 1:250 was computed and selected for the wind tunnel measurements. Hence, the base height of the building model was 45 mm, and the diameter of each dome on the roof was D = 35 mm. Accordingly, the total height of the model was H_b = 62.5 mm, with a total blockage ratio of 2.2% in the tunnel. Therefore, the model simulates the field scale building. Using the total model height and free stream velocity of 10 m/s, the flow Reynolds number was 43,000. The influence of Reynolds number on the flow around building structure is described in the following sections. Longitudinal velocities were measured using a single split-fiber hot-film probe (Dantec 55R55) of 3 mm long and 200 μm diameter. The probe has two parallel nickel films deposited on the same quartz fiber and is covered with a 0.5 μm quartz coating.

2.1.2. Measurement technique

The Dantec 55R55 probe is capable of measuring the instantaneous velocity and direction in gas flows (Dantecdynamics), and it is well suited for velocity measurement around buildings model with dome array roofs at the symmetry plane [29,31].

The Karman-vortex method described by Ardekani [36] was used to calibrate each sensor in the wind tunnel. Details of the calibration technique were presented in the study of Tavakol et al. [29] and Rahmatmand et al. [31]. For each set of experiments, a constant free stream velocity was attained and measured by using a pitot tube. Also, as described by Rahmatmand et al. [31], the uniformity of the generated boundary layer profile was assured by checking the velocity profiles at several sections in the spanwise direction. According to the previous studies of Tavakol et al. [29] and Rahmatmand et al. [31], the maximum uncertainties in measurements were 3% and 7% for velocity and RMS velocity, respectively.

2.2. Computational model

2.2.1. Governing equations

For numerical simulation of turbulent airflow around the building model, both LES and SRANS with the RNG k-ε turbulence model of Yakhot et al. [37] were used. For the SRANS, the governing equations are the time-averaged continuity and momentum equations. The full set of governing equations of the SRANS model was presented in the study of Haghighifard et al. [38], and therefore is not repeated here for brevity.

In the LES approach, spatial filtering is used, and the large scale flow fluctuations are resolved, and the smaller subgrid scales (SGS) are appropriately modeled. The governing equations of LES are the filtered continuity and Navier-Stokes equations. These are,

$$\frac{\partial \overline{u}_i}{\partial x_i} = 0 \tag{1}$$

$$\frac{\partial \overline{u}_i}{\partial t} + \overline{u}_j \frac{\partial \overline{u}_i}{\partial x_j} = -\frac{\partial\left(\overline{P}\delta_{ij} + \tau_{ij}\right)}{\partial x_j} + \nu \frac{\partial^2 \overline{u}_i}{\partial x_j \partial x_j} \tag{2}$$

where $\overline{u}_i$ designates the resolved velocity components, $\overline{P} = \frac{\overline{p}}{\rho}$ with $\overline{p}$ is the mean pressure, ρ is the fluid density, τ_{ij} is called the SGS stress tensor, Germano et al. [39],

$$\tau_{ij} = \overline{u_i u_j} - \overline{u}_i \overline{u}_j \tag{3}$$

For SGS modeling, the localized dynamic subgrid kinetic energy model (DKM) of Kim and Menon [40] was used. Tavakol et al. [22] showed that this model provides the most accurate predictions for velocity and turbulence intensity profiles around the model of a wall-mounted hemisphere, among other SGS models. To find SGS eddy viscosity in the DKM model, an additional filtered transport equation for subgrid kinetic energy, k_{SGS} is solved. That is,

$$k_{SGS} = \frac{1}{2}\left(\overline{u_k u_k} - \overline{u}_k \overline{u}_k\right) \tag{4}$$

$$\frac{\partial k_{SGS}}{\partial t} + \overline{u}_i \frac{\partial k_{SGS}}{\partial x_i} = \frac{\partial}{\partial x_i}\left(\left(\nu + \nu_t\right)\frac{\partial k_{SGS}}{\partial x_i}\right) - \tau_{ij}\frac{\partial \overline{u}_i}{\partial x_j} - \varepsilon_{SGS} \tag{5}$$

The subgrid tensor is

$$\tau_{ij} - \frac{2}{3}\delta_{ij}k_{SGS} = -2\nu_t \overline{S}_{ij} = -2C_\tau \overline{\Delta} k_{SGS}^{1/2} \overline{S}_{ij} \tag{6}$$

In Eq. (6),δ_{ij} denotes Kronecker delta, $\overline{S}_{ij}$ is the resolved-scale strain rate tensor, and ν_t is the SGS eddy viscosity. The resolved-scale strain rate tensor is given as,

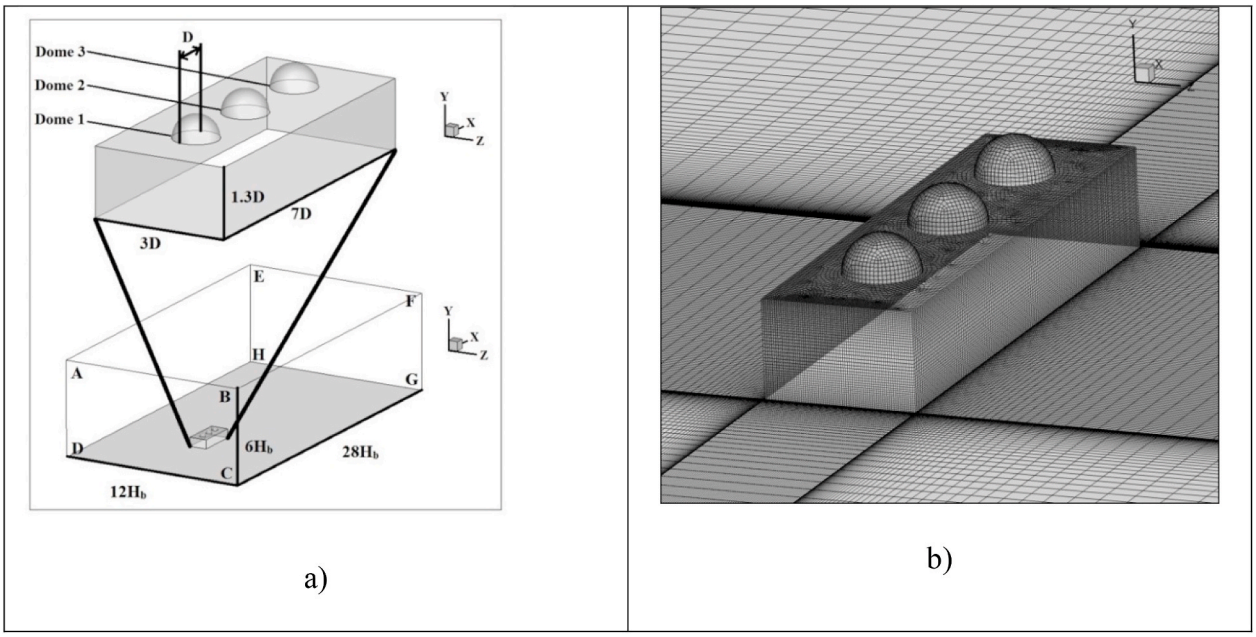

Fig. 4. a) Computational domain and relative dimensions. b) Basic grid arrangement around the building model.

$$\overline{S}_{ij} = \frac{1}{2}\left(\frac{\partial \overline{u}_i}{\partial x_j} + \frac{\partial \overline{u}_j}{\partial x_i}\right) \tag{7}$$

In Eq. (6) $\overline{\Delta}$ is the grid filter and ε_{SGS} is the dissipation term and is given by,

$$\varepsilon_{SGS} = \frac{C_\varepsilon k_{SGS}^{3/2}}{\overline{\Delta}} \tag{8}$$

C_τ and C_ε are the model constants, and they are determined dynamically during computations by applying a test grid filter suggested by Kim and Menon [40]. The test filter is typically $\widehat{\Delta} = 2\overline{\Delta}$, and it should be employed to construct the test-scale field similar to the classical Germano et al. [39] dynamic closure procedure. Accordingly, C_τ was estimated by employing the least-square method [41] as:

$$C_\tau = \frac{1}{2}\frac{L_{ij}\sigma_{ij}}{\sigma_{lm}\sigma_{lm}} \tag{9}$$

$$L_{ij} = -2C_\tau \hat{\Delta} k_{test}^{\frac{1}{2}} \widehat{\overline{S}_{ij}} + \frac{1}{3}\delta_{ij}L_{kk} \tag{10}$$

$$\sigma_{ij} = -\hat{\Delta} k_{test}^{\frac{1}{2}} \widehat{\overline{S}_{ij}} \tag{11}$$

Here the resolved kinetic energy k_{test} and σ_{ij} were computed at the test filter level. It is worth mentioning that some instability problems occur in the original Dynamic Smagorinsky Model (DSM) when the denominator in Eq. (9) locally tends to zero. The DKM formulation of Kim and Menon [40] that is used in the present study avoids the instability issue in the dynamic calculation of the model parameter, C_τ.

2.2.2. Computational domain, grid, and boundary conditions

The computational domain and boundary conditions for numerical simulations were selected according to recommendations of the Architectural Institute of Japan (AIJ). Accordingly, the computational domain was constructed with a distance of $5H_b$ from the building to the top of the domain and the side boundaries. The distance between the building and the upstream and downstream boundaries was $4H_b$ and $21H_b$, respectively. The computational domain and the relative dimensions are shown in Fig. 4a. While the computational domain is developed for the field-scale application, comparison with the wind tunnel data will not be affected due to the small blockage of the model in the tunnel. The computational domain was discretized with multi-block structured grids consist of 1,700,000, 3,300,000 and 5,400,000 cells. High-resolution grids were generated near the building on the top roof and in the region between the domes, as shown in Fig. 4b.

The boundary conditions include velocity inlet at plane ABCD, symmetry at the lateral planes BFGC, AEHD, and top boundary AEFB, and the pressure outlet with zero-gauge static pressure at the outlet boundary. For other boundaries DHGC and on the building model surface, the no-slip wall boundary condition was used. For the near-wall treatment, the sand grain roughness was set to zero for the bottom of the computational domain and on the building walls and domes' surfaces. For Re = 43,000, the range of non-dimensional wall distances, y^+, in the region around the building and over the domes were $7 < y^+ < 70$, $3 < y^+ < 20$, $1.82 < y^+ < 7$, respectively, for the coarse, basic, and fine grids. For the fine grid used in the study, about 90% of y^+ values were lower than 5. For very fine near-wall grids ($y^+ < 11.25$), the ANSYS-Fluent employs the laminar stress relationship to resolve the viscous sublayer:

$$\frac{\overline{u}}{u^*} = \frac{\rho u^* y}{\mu} \tag{12}$$

However, if the near-wall grids are coarse, ($y^+ > 11.25$), the law of the wall is employed:

$$\frac{\overline{u}}{u^*} = \frac{1}{\kappa} lnE\left(\frac{\rho u^* y}{\mu}\right) \tag{13}$$

Here $\kappa = 0.4$ denotes the von Karman constant and $E = 9.793$. Comparison of our results with the wind tunnel data in section 3 confirms that the near-wall boundary conditions given by (12) and (13) are suitable for predicting the near-wall mean velocity and streamwise fluctuating velocity with the fine grid.

For the inlet boundary, plane ABCD in Fig. 4a, a power-law velocity profile given as,

$$\frac{\overline{u}(y)}{U_{ref}} = \left[\frac{y}{H_{ref}}\right]^{\alpha} \tag{14}$$

was imposed. This is the same as the mean velocity profile measured at the upstream part of the model in the wind tunnel. Such an inlet velocity

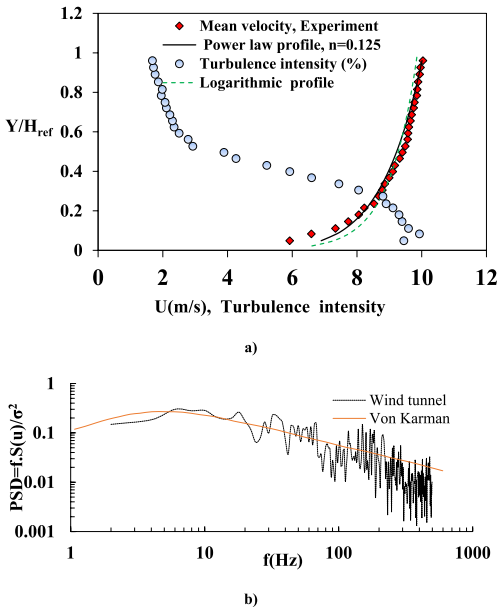

Fig. 5. a) Inlet streamwise velocity and turbulence intensity profiles in the wind tunnel and inlet profile used in the numerical simulations. b) Power spectral density (PSD) of streamwise velocity fluctuations measured in the wind tunnel and the von Karman spectrum.

profile is appropriate for the ABL in desert areas White [42], Haghighifard et al. [38]. Fig. 5a indicates the fitted power law and logarithmic velocity profiles compared to the mean streamwise velocity profile measured in the wind tunnel. Accordingly, the boundary layer thickness was about $H_{ref} = 3H_b$. It should be noted that the log law profile ($\overline{u}(y) = \frac{u^*_{ABL}}{\kappa}\ln\left(\frac{y+y_0}{y_0}\right)$), gives the value of $u^*_{ABL} = 0.36$ m/s for the reduced scale model at $H_{ref} = 0.186$ m with the reference velocity of 10 m/s. Another important parameter is the aerodynamic roughness height y_o, which was deduced from a fitting formula using the measured velocity profile in the wind tunnel [43]. The corresponding roughness height was $y_0 = 0.0015$ m. Fig. 5a also shows the distribution of turbulence intensity at the inlet boundary as measured in the wind tunnel in the upstream region of the model. Accordingly, the maximum turbulence intensity in the wind tunnel was 10%, which is slightly lower than $Tu_{max} = 12\%$ in the study of [31]. In the study of De Bortoli et al. [35], it was shown that for part-depth simulation of ABL and with the present power-law exponent $0.09 < n = 0.125 < 0.14$, the maximum level of turbulence intensity should be between 10 and 12%.

In Fig. 5b, the measured power spectrum of streamwise velocity fluctuations at the Y = 0.1 m wind tunnel scale is shown, and the results are compared with the von Karman spectrum across the frequency range. It is seen that the experimental power spectrum shows good agreement with the von Karman spectrum, whereas the wind tunnel data decrease faster in the high-frequency region [35].

When the vertical distribution of turbulence kinetic energy is not available from the wind tunnel data, based on the recommendation of the AIJ guideline (Tominaga et al. [44]), the inlet turbulence kinetic energy (k), and the turbulent dissipation rate (ε) profiles were calculated using,

$$k(y) = (\overline{u}(y) \times I(y))^2 \tag{15}$$

$$\varepsilon(y) \cong P_k(y) \cong C_\mu^{0.5} k(y) \frac{d\overline{u}(y)}{dy} \tag{16}$$

where I(y) denotes the measured values of turbulence intensity, and $C_\mu = 0.09$ is an empirical constant. It is worth noting that the inlet turbulence dissipation rate, Eq. (16) was compared with the $\varepsilon(y) = \frac{(u^*_{ABL})^3}{\kappa(y+y_0)}$ calculated based on the friction velocity and the roughness height, and only slight differences in the near-wall region were observed.

For the LES, in addition to the mean velocity profile, a time-dependent inlet velocity profile should be generated. For generating the velocity fluctuations at the inlet, the procedure proposed by Sergent [45] was employed. Accordingly, in this method, a perturbation is added to the mean velocity profile using a two-dimensional fluctuating vorticity field with a certain distribution. The intensity of velocity fluctuations was adjusted with a given formula for circulation, Γ_i, which can be identified with turbulence kinetic energy distribution at the inlet plane [45]. Accordingly, the circulation can be expressed as:

$$\Gamma_i = 4\sqrt{\frac{\pi S k(x_i)}{3n[2\ln(3) - 3\ln(2)]}} \tag{17}$$

where S in the inlet surface, k is the turbulence kinetic energy, x_i is the center of the vortex, and n is the number of vortices. At first, the vortices are distributed randomly, and a characteristic time scale of $\tau = \frac{k}{\varepsilon}$ is defined for each vortex. If the vortex lifetime is exceeded, then the vortex disappears, and a new vortex is generated randomly [45]. Then, with a random walk at the inlet plane, the velocity fluctuation is developed in time. In an earlier study, Tavakol et al. [22] and van Hooff et al. [46] used this method successfully in their LES of wind flow around a wall-mounted hemisphere and cross ventilation flow around an isolated building. The horizontal homogeneity of the inlet velocity profile was checked in an empty computational domain. A small near-wall acceleration was observed for the incident mean velocity profile at the building location.

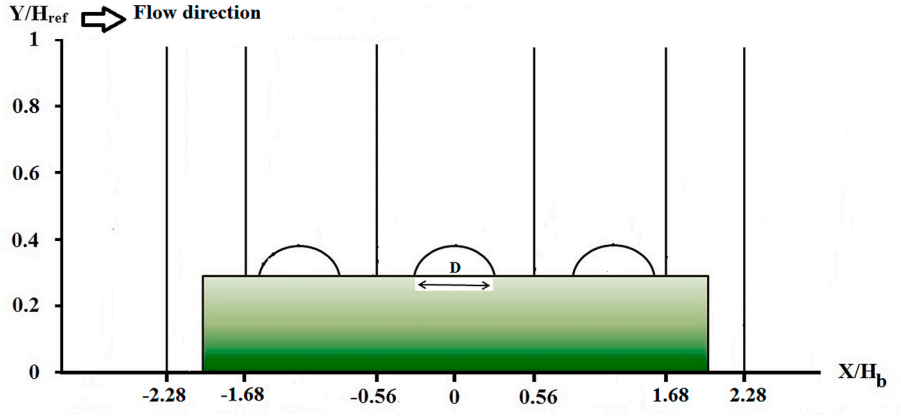

Fig. 6. Locations of measurements on the symmetry plane around the building model in the wind tunnel.

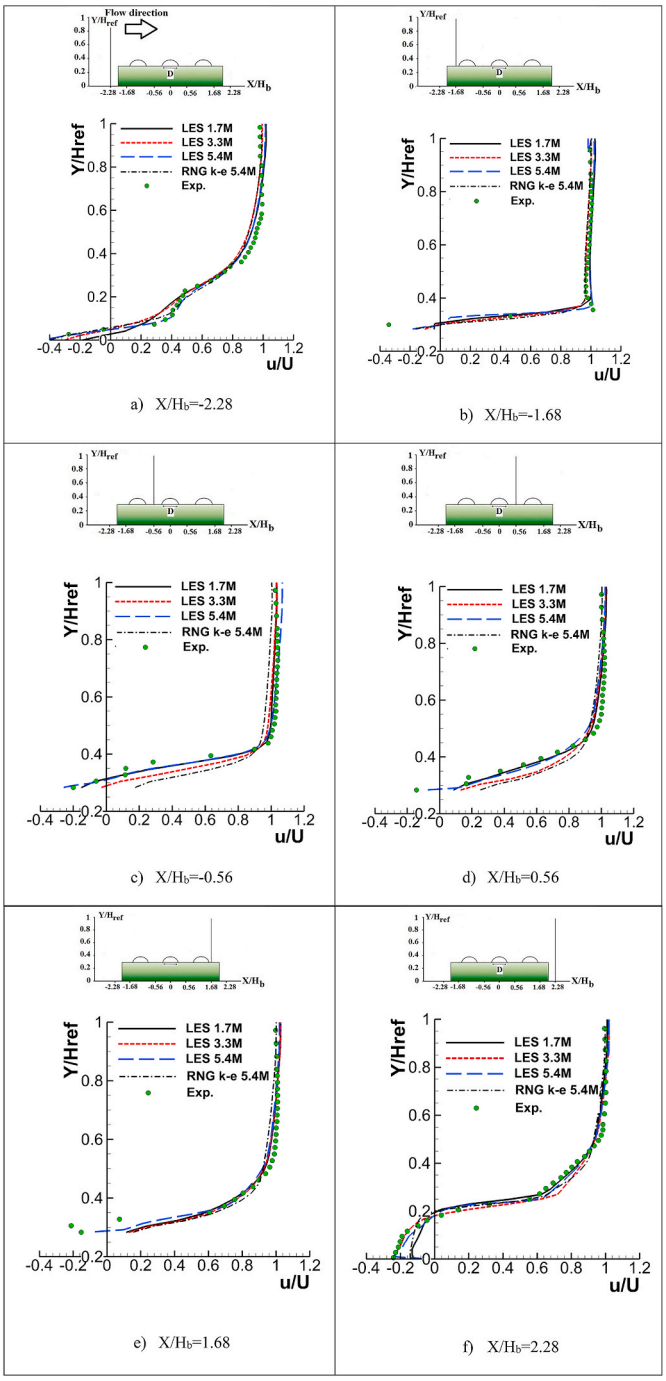

Fig. 7. Comparison of the LES of non-dimensional streamwise velocity at various sections at the model symmetry plane for various grid resolutions with the experimental data at Re = 43,000.

2.2.3. Numerical solution

The discretized governing equations were solved by the finite volume method using the Ansys-Fluent 17 software. The filtered momentum equations are discretized using the bounded central-difference scheme, and pressure interpolation used was second-order accurate. The SIMPLE algorithm was used for the pressure velocity coupling, and the second-order implicit method was used for time integration. To obtain statistically-stationary results, the mean velocity and mean pressure were monitored at various locations inside the computational domain. The LES results presented here were collected over 50 flow-through times in the computational domain. These simulations were performed on an Intel 2.4 GHz with six cores and 32 GB operating memory. The maximum computational time for one set of runs was about 1500 CPU hours. For grid–independency tests, the LES simulations were conducted on coarse, basic, and fine grids.

For computations, the converged solution was assumed when the maximum absolute value of continuity and momentum residuals decreased to 10^{-6}. The velocity and pressure were monitored at several locations in the computational domain to ensure solution convergence. In LES, the grid size in the computational domain and proper time step size are important parameters to achieve satisfactory results. According to Tavakol et al. [22], the grid filter should be at least one-tenth of large scales, $L = \frac{k^{3/2}}{\varepsilon}$, and for proper modeling, it should be selected between the Taylor microscale and the Kolmogorov length scale. In the current study, the grid filter is defined as $\Delta = (\Delta x.\Delta y.\Delta z)^{1/3}$, where Δx, Δy, Δz are grid size in the x, y, z directions, respectively.

To find proper time step size for the numerical simulations, preliminary numerical simulations were conducted, and important time scales were computed for large eddies, $T_L = \frac{k}{\varepsilon}$, Taylor time scale, $\lambda_t = \left(\frac{15\nu}{\varepsilon}\right)^{1/2}$ and Kolmogorov time scale, $\tau_\eta = \left(\frac{\nu}{\varepsilon}\right)^{1/2}$. The time step size of $\Delta t = 0.0008\ s$ is selected for unsteady simulation with LES, which is much less than the time scale of large scales and close to the Taylor micro time scales [22]. Also, using this time step size, the maximum CFL number of approximately one was attained with the basic and fine grids. Applying the implicit time discretization schemes and the above mentioned CFL condition allow the computation of the required time interval with fewer steps and acceptable accuracy [22,46]).

3. Results and discussion

The hot-film anemometer was used in the measurements of the velocity in the wind tunnel. Fig. 6 indicates the locations of measurements at the symmetry plane of the building model. For measurement, the probe was placed near the walls and moved upward, far from the model.

3.1. Time-averaged results

Time-averaged results of the flow around the building are presented in this section. For illustration, the LES instantaneous flow was averaged through 50 dimensionless times, $t^* = \frac{\Delta t.U}{H_b}$, with $U = 10$ m/s. The data sampling for unsteady statistics was started after an initial stage of simulations with a period of 50 dimensionless times. This period is selected to ensure the accuracy of the averaged flow statistics similar to Ref. [22] for flow around a surface-mounted hemisphere.

Fig. 7 compares the streamwise velocity profiles as predicted by the RNG k-ε model with the fine grid and the LES with the DKM SGS model using different meshes with the experimental data measured in the wind tunnel locations shown in Fig. 6. It is seen that there are three reversed flow regions around the building model. In front of the building, a reversed flow region is formed due to the separation of incoming atmospheric boundary layer flow. Besides, upstream of the first dome and downstream of all domes on the roof, reversed flow zones are observed. These are because of flow separation from the leading edge of the building and the separation over the backside of the dome surfaces. Fig. 7a shows an excellent agreement of the fine-grid LES with the experimental data in front of the building. In addition, satisfactory agreements can be seen for the numerical solution with coarse and basic grids for $Y/H_{ref}>0.2$. At this cross-section, the prediction of the RNG k-ε model is also satisfactory, and the LES with the fine grid and the RNG k-ε model provides almost identical velocity profiles.

The comparisons between the non-dimensional streamwise velocity as predicted by the LES and the experimental data over the roof is shown in Fig. 7b–e. This figure shows that upstream of the first dome, the LES

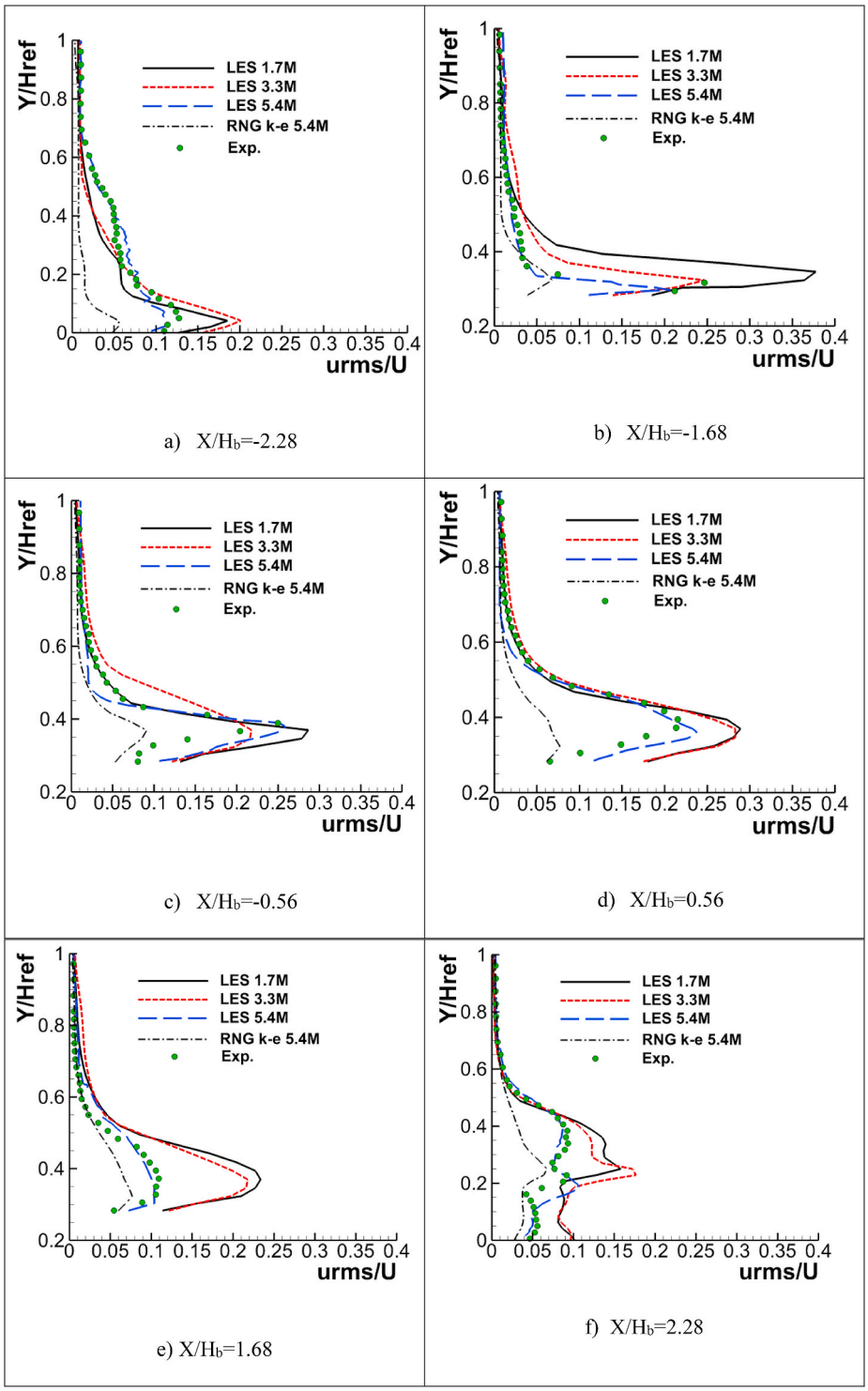

Fig. 8. Comparison of the predicted non-dimensional fluctuating velocity at various sections around the model symmetry plane for various grid resolutions with the experimental data at Re = 43,000.

simulation slightly under-predicts the reversed flow velocity near the roof. However, all simulations captured the large velocity gradient in this region. Over the roof and between domes 1 and 2, the fine-grid LES results are in fair agreement with the experimental data, while the results obtained with basic and coarse grids are also satisfactory. Over the building and at the leeward side of the building, the RNG k-ε model does not predict the reversed flow correctly that deviates from the experimental data. Fig. 7c indicates that the RNG k-ε model could not accurately predict the near-wall reversed velocity along the line $X/H_b = -0.56$. Quantitatively, the RNG k-ε model predicts the non-dimensional velocity $u/U = 0.16$ while the measured value non-dimensional velocity is around −0.2.

Further downstream, between domes 2 and 3 and downstream of dome 3, the LES with coarse and basic grids fail to capture the reversed flow region near the roof. At the leeward side of the building, both LES and experimental data illustrate a reversed flow zone between $0 < Y/H_{ref} < 0.2$. LES with the fine grid shows the best performance in predicting the velocity profile in the separated region behind the building

Table 2
Validation metrics, the factor of two of observations FAC2, fractional bias FB, and normalized mean square error NMSE.

Parameter	Mean velocity (u)		RMS of streamwise velocity (u_{rms})		
	NMSE	FAC2	FB	NMSE	FAC2
LES coarse grid	0.015	0.846	−0.25	0.328	0.769
LES basic grid	0.007	0.923	−0.15	0.324	0.846
LES fine grid	0.006	1	0.05	0.018	1
RNG k-ε	0.1	0.45	0.43	0.35	0.4

model. Also, the result of LES with the basic grid seems to be satisfactory. In summary, results indicate that the LES with proper grid resolution is an accurate scheme for capturing the transient flow features and predicting the streamwise velocity profile around the building model. Prediction of the mean velocity field is important for designing a proper air condition system and using the passive ventilation benefits of domes with an air vent. Haghighifard et al. [38] also showed that the hot-spot sites for the deposition of aerosol particles are located at the upstream and downstream recirculation zones around a building model. Hence, the correct estimation of the reversed flow zones around the building model is critical for predicting particles' deposition pattern around the structure accurately.

Fig. 8 shows the root-mean-square (RMS) streamwise velocity fluctuations, $(\overline{u'u'})^{1/2}$, normalized by free stream velocity at the reference height as predicted by different computational grids. The wind tunnel data are also shown in this figure for comparison. Fig. 8a shows that upstream of the building, the maximum value of streamwise velocity fluctuations occurred at $Y/H_{ref} = 0.06$. The LES with coarse and basic grids over-predicted the peak streamwise velocity fluctuations compared to the experimental data. However, the prediction of LES with the fine grid shows much better agreement with the experimental data. Furthermore, LES with coarse and basic grids under-predicted the streamwise velocity fluctuations in the range of $0.2 < Y/H_{ref} < 0.7$. Fig. 8 also shows that the RNG k-ε model could not capture the peak of streamwise velocity fluctuations in front of the building model and on the building roof.

The maximum level of streamwise velocity fluctuations is observed to occur over the building rooftop. Upstream of the first dome, the LES with the fine grid satisfactorily predicts the streamwise velocity fluctuations. Again, the LES with the coarse grid overestimated the streamwise

Table 3
Length of upstream separation and downstream reattachment computed with various grids at symmetry plane for Re = 43,000.

Case	X_{us}/H_b	X_{dr}/H_b
LES coarse grid	1.8	1.7
LES basic grid	1.6	1.6
LES fine grid	1.2	1.5
RNG k-ε	1.7	1.2
Exp.	1.1	1.4

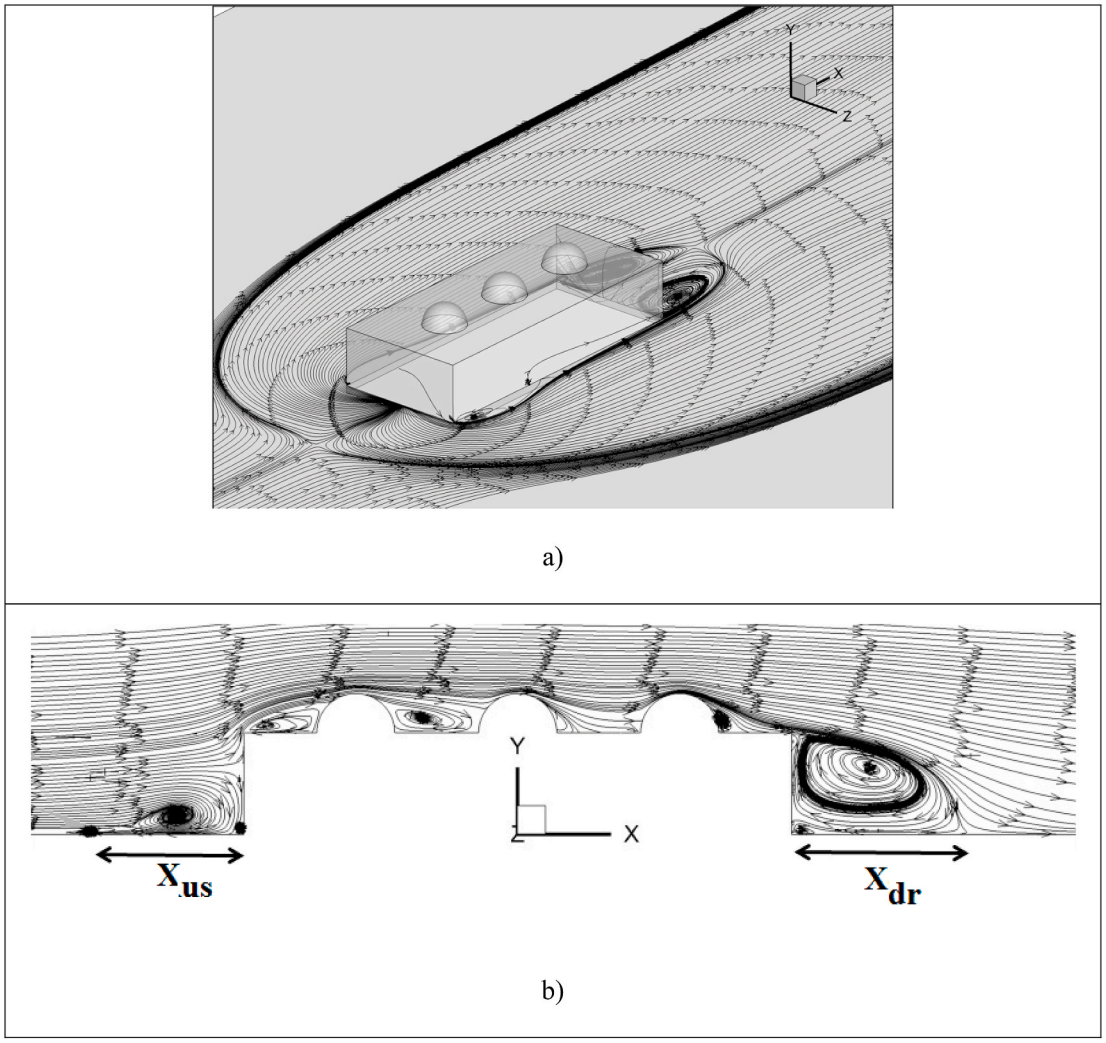

Fig. 9. Time-averaged streamlines obtained from the large-eddy simulations with fine grid, a) near the bottom wall, b) at the symmetry plane z = 0.

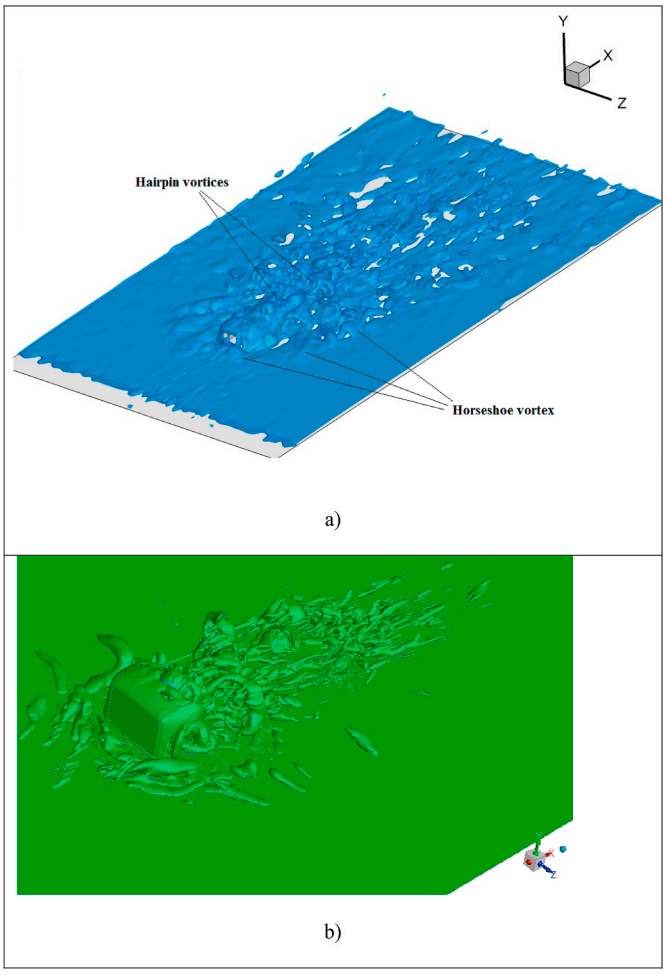

Fig. 10. a) Instantaneous iso-surface of vorticity magnitude $\Omega.H_b/U_\infty = 0.625$ at $t.U_\infty/H_b = 320$ in the computational domain. b) Instantaneous iso-surface of Q. $H_b/U_\infty = 300$ at $t.U_\infty/H_b = 320$ around the building.

velocity fluctuations due to insufficient grid resolution. This is also the case for X/H between the domes. In the leeward side of the building, two peaks in the streamwise velocity fluctuation profile can be identified that are captured by the high-resolution grid reasonably well. In conclusion, an accurate prediction of fluctuating velocity requires a high-resolution grid around the building model even with LES, which is an advanced numerical model. The fluctuating velocity field is important for the prediction of fluctuating wind load on the building structure and prediction of dispersion and deposition of dust particles.

To quantitatively evaluate the accuracy of the numerical simulations of the streamwise velocity and fluctuating velocity profiles, the validation metrics are calculated. They are the factor of two observations (*FAC2*), fractional bias (*FB*), and normalized mean square error (NMSE).

The *FAC2* indicates the fraction of the predicted results in a factor of 2 of the corresponding measured values (Schatzmann et al. [47]). *FB* is a measure of mean bias in the predictions, and the *NMSE* is a measure of data scatter and contains both systematic and random errors. These metrics are defined as:

$$\mathrm{FAC2} = \frac{1}{N}\sum_{i=1}^{N} n_i\ ,\ n_i = \begin{cases} 1\ if\ 0.5 \le \dfrac{P_i}{Q_i} \le 2 \\ 0 \quad otherwise \end{cases} \tag{18}$$

$$\mathrm{FB} = \frac{[O] - [\mathrm{P}]}{0.5([\mathrm{O}] + [\mathrm{P}])} \tag{19}$$

$$\mathrm{NMSE} = \frac{\left[(O_i - P_i)^2\right]}{[O_i][P_i]} \tag{20}$$

Here P_i indicates the CFD prediction, O_i is the measured value, n is the number of measurement locations, and brackets indicate averaging over all data points.

According to Ref. [47], FB defines a systematic difference between the numerical simulation results and the experimental data, and NMSE shows systematic and random discrepancies between predictions and measurements.

The value of 1.0 for FAC2 and 0.0 for FB and NMSE denote perfect agreement between computations and experimental data. Table 2 shows the present calculations for the validation metrics.

According to Schatzmman et al. [47] and Tominaga and Stathopoulos [48], the acceptable values for validation metrics are $FAC2>0.5$, $|F2B|<0.3$, $NMSE<4$. That is, a *FAC2* higher than 50%, the mean bias within ±30% of the mean represents acceptable accuracy of numerical simulations. Table 2 shows that the LES with the fine grid exhibit a good agreement with the wind tunnel data for both mean velocity and fluctuating velocity profiles. This highlights the importance of proper grid resolution in the near-wall region and the spanwise direction to accurately capture the reversed flow region around the domes and the peak RMS velocity fluctuations. Table 2 also shows that the RNG k-ε model predictions are not satisfactory, although a high-resolution grid was used. It is conjectured that this is due to neglecting the unsteady fluctuations around the building model and the isotropic turbulence model.

Fig. 9a indicates the time-averaged streamlines around the building model near the bottom wall. The formation of a large horseshoe vortex in front of the building is observable, extending to far downstream regions. Furthermore, a reversed flow zone appears due to flow separation from the building lateral walls. In the building's leeward side, two counter-rotating vortices are formed because of flow separation from the building trailing edge. In Fig. 9b, the time-averaged streamlines at symmetry plane z = 0 are plotted. Formation of reversed flow zone in front of the building due to the separation of the incoming atmospheric boundary layer, flow separation from the leading edge of the building, and flow separation over the domes are observable in Fig. 9b.

The upstream separation length, X_{us}, and the downstream reattachment length, X_{dr}, as predicted by the large-eddy simulations, are listed in Table 3 and are compared to the wind tunnel data.

3.2. Unsteady results

In this section, the dynamics of flow patterns and physical flow characteristics around the building model are presented and discussed. The Iso-surface of vorticity magnitude and velocity spectrum at a point in the wake of the building model are presented and discussed. An instantaneous sample flow and vortex structure around the model obtained with the large eddy simulation is illustrated in Fig. 10. In the windward side of the building, the accumulation of vorticity is observed, which forms the horseshoe vortex that extends to the downstream region of the building model. Upstream development of horseshoe vortex results in the boundary layer separation from the surface due to the building's blockage, as shown in Fig. 10a.

Over the building, flow separation from the leading edge of the building and over the domes caused the formation of arc typed vortices, and vortex roll-up extends downstream to the wake behind the building. Large and complex vortical structures are formed behind the building due to the interaction between the rolled-up vortices and the horseshoe vortex. Such elongated vortices form the hairpin vortical structures of different sizes in the leeward side of the building. Further downstream, smaller vortices can be observed near the ground, characterized by the turbulent boundary layer in the building's downstream region. Fig. 10b shows the instantaneous 3D vortical structures extracted by the Q criterion, where Q is defined as the second invariant of the velocity

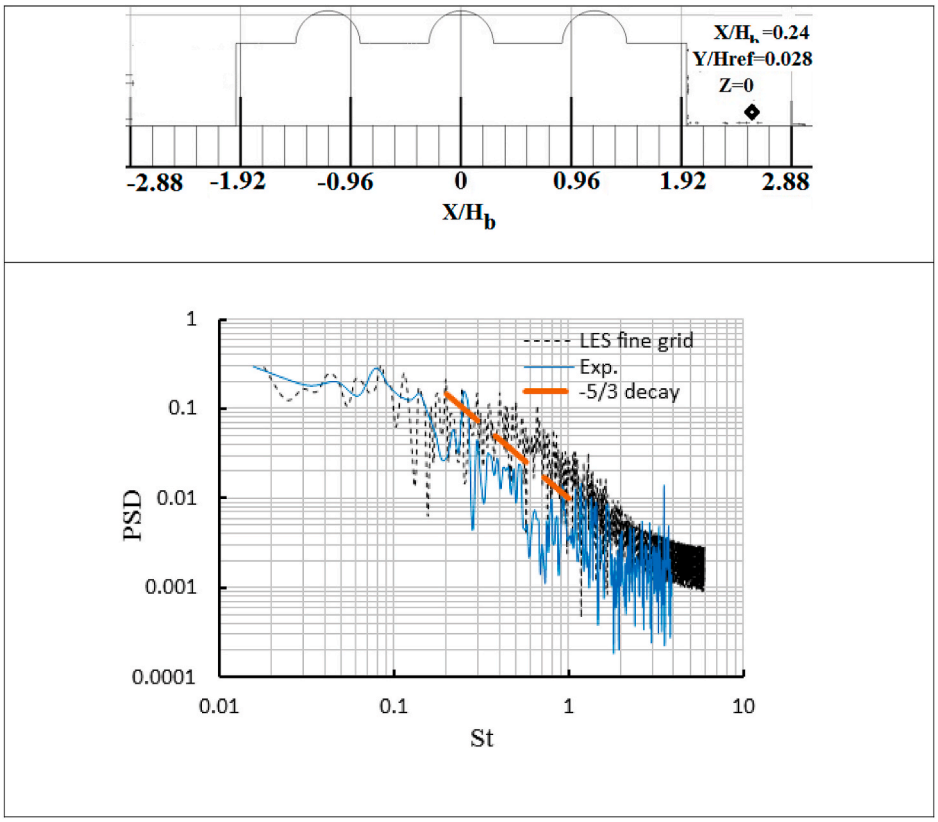

Fig. 11. Comparison between the streamwise velocity spectra obtained with LES and wind tunnel measurement in the wake of the building model. The Kolmogorov −5/3 law is also shown in this figure for comparison.

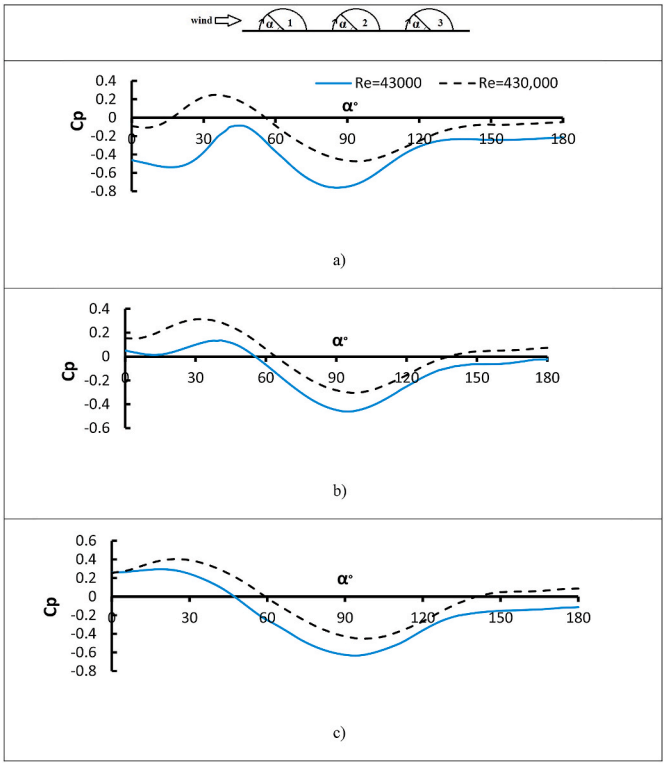

Fig. 12. Comparison of the mean pressure coefficient distributions over the domes as predicted with the LES for low and high Reynolds numbers. a) First dome. b) Second dome. c) Third dome.

gradient tensor [49]. Using the Q parameter, it is possible to highlight the regions with high vorticity concentration in the flow field. Regions with high vorticity concentration are observed in front of the building model, near the sidewalls, over the domes, and in the leeward side of the model due to flow separation in front of the model and over the domes.

The streamwise velocity spectrum at a sample point located in the leeward side of the model is plotted in Fig. 11. For this plot, the data were collected over a time period of about 5 min with a sampling rate of approximately 1 kHz with the hot film probe. This plot identifies the vortex shedding process in the wake of the model and specifies the instantaneous vortices traveling in this region. The power spectral density (PSD $= \frac{fS(f)}{\sigma_u^2}$) of instantaneous streamwise velocity obtained with the fine grid is compared with the wind tunnel data. At this location, experimental data shows the maximum PSD at $St = 0.08$, with $St = \frac{fH_b}{U}$, corresponding to the shedding frequency of $f = 12.8$ Hz. This peak can also be observed in the LES results at a slightly higher frequency. Wood et al. [23] reported the shedding frequency of f = 9.2 Hz at a point located at the symmetry plane in the leeward side of a surface-mounted hemisphere for $Re_D = 50{,}000$, based on free stream velocity and hemisphere diameter. Fig. 11 also shows the decay of the energy spectrum proportional to the −5/3 power of the non-dimensional frequency ($St^{-5/3}$) in the Kolmogorov range.

3.3. Effect of flow Reynolds number

In this section, the effect of Reynolds number on the flow around the building model is presented and discussed. The present building model in the current study leads a fixed separation point at the leading edge of the model and several separation points over the domes. The LES results show that the separation point locations on the symmetry plane over the dome surfaces are a function of flow Reynolds number and incoming turbulence intensity. This observation was also reported by Tavakol

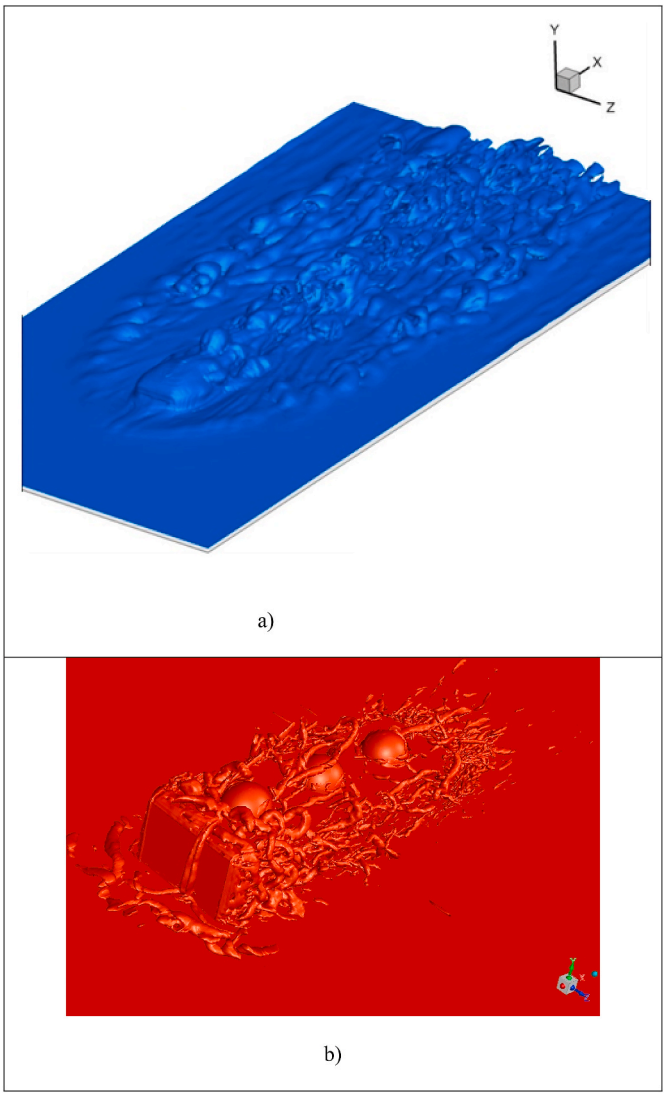

Fig. 13. a) Iso-surface of vorticity magnitude $\Omega \cdot H_b/U_\infty = 0.625$ at $t \cdot U_\infty/H_b = 320$ around the building. b) Instantaneous iso-surface of $Q \cdot H_b/U_\infty = 300$ at $t \cdot U_\infty/H_b = 320$ around the building.

et al. [29] and Meroney et al. [11]. Therefore, to assess the Reynolds number's influence on the flow pattern around the domes, an additional numerical simulation is performed for a model with Re = 430,000. In this case, the size of the model and the computational domain is increased by a factor of 10 compared to the lower Re case. The solution method, boundary conditions, and discretization scheme are similar to the main computations except for the grid size. Here, a computational grid containing approximately 8 million grid cells is used. The value of non-dimensional wall distance, y^+ for 90% of near-wall cells around the model was less than 5.

Fig. 12 compares the pressure coefficient distribution over the domes for Re = 43,000 and Re = 430,000. The mean pressure coefficient is defined as $C_p = \frac{P-P_{ref}}{\rho U^2/2}$, where P_{ref} denotes the reference pressure at the inlet plane of the computational domain. The same trends of variation can be observed for pressure distributions over the domes for these two Reynolds numbers, however, with different pressure coefficient magnitudes. For the first dome and at Re = 43,000, a negative pressure coefficient is observed over the dome because the first dome is located in the separated region from the leading edge of the building model. Another observation from Fig. 12a is that the pressure recovery is at $0^\circ < \alpha < 40^\circ$ and $90^\circ < \alpha < 180^\circ$ over the first dome for both Reynolds numbers. At Re = 430,000 over the first dome, a positive pressure is seen at $18^\circ < \alpha < 48^\circ$. Over the first dome, the peak pressure occurs at $\alpha = 47^\circ$ with Cp = −0.1 and $\alpha = 36^\circ$ with Cp = 0.25, respectively, for the simulated flows at low and high Reynolds numbers. For Re = 430,000 and the second and third domes, the pressure recovery in the wake causes a positive pressure coefficient at angle $140^\circ < \alpha < 180^\circ$. Also, the peak suction is observed for Re = 43,000 over the first dome near the dome apex with Cp = −0.76. The maximum pressure over the second and third domes is seen with Cp = 0.31 and Cp = 0.39 at $\alpha = 35^\circ$ and $\alpha = 30^\circ$, respectively.

The peak suctions over the second and third domes with Cp = −0.46 and Cp = −0.63 are observed near the dome's apex for Re = 43,000. Evidently, the pressure distribution over the domes is Reynolds number dependent, indicating that the separation-reattachment process varies with Reynolds number. As noted before, one of the advantages of the domed roofs is their capability for natural ventilation when they have an air vent on their apex. As air flows over a dome, at the dome apex, the air velocity increases, while the pressure decreases. The low pressure over the apex causes the air under the dome to flow out through the vent, providing passive ventilation. Comparison of the peak suction over the array of three domes for the two Reynolds numbers that were studied reveals that the airflow over the first dome vent is higher than the other two domes. Hence, a larger vent may be installed on the first dome apex than the other domes in the array for more effective natural ventilation.

For high Reynolds number flow with Re = 430,000, the 3-D instantaneous vortex structure around the building is presented in Fig. 13a. This figure indicates that a standing horseshoe vortex forms in the building's vicinity that continues downstream of the building. Further downstream, the growth of hairpin vortices is observed, and this region is followed by the formation of multiple secondary hairpin vortices. For Re = 430,000, Fig. 13b specifies the instantaneous vortical structure at $t \cdot U_\infty/H_b = 320$ identified by the Q criterion. The vorticity concentration in front of the building, over the building roof, around the sidewalls, and behind the building is seen in this figure.

3.4. Aerodynamic interference of the domes

As noted before, for an array of bluff bodies mounted inline in a flow field, the disturbance generated by the upstream obstacle affects the structure of flow around the downstream obstacles. In this section, the influence of domes on the airflow field on the roof and around the building is examined. For Re = 43,000, Fig. 14a shows the mean streamlines at the building's symmetry plane and highlights the separation point over the domes. For better illustration, the RMS streamwise velocity contours are also plotted in this figure. It is seen that the separation points over the three domes are located, respectively, at angles of $\theta_{S1} = 92^\circ$, $\theta_{S2} = 103^\circ$, and $\theta_{S3} = 107^\circ$. Clearly, the separation point moves further downstream for the second and third domes. This reduces the size of recirculation zones behind the second and third domes. For a single wall-mounted hemisphere in a turbulent atmospheric boundary layer flow, Tavakol et al. [29] reported $\theta_S = 108^\circ$ for $Re_H = UH/\nu = 32,000$, based on the hemisphere height, and Savory and Toy [5,21] reported $\theta_S = 105–110^\circ$ for $Re_H = 70,000$.

Fig. 14b shows the mean streamlines and separation points over the domes for Re = 430,000. In this case, the same trend is observed for the flow pattern around the building model, including the upstream reversed flow zones in the windward side and leeward side of the model and the reversed flow zones behind the domes. This figure shows that the reversed flow zone behind the domes is smaller than the lower Re = 43,000 case. In addition, the center of the vortex in the upstream part of the model for Re = 430,000 is located at a distance further away from the leading edge of the model compared to the low Reynolds number flow case. The separation points over the domes are located at angles of $\theta_{S1} = 122^\circ$, $\theta_{S2} = 135^\circ$, and $\theta_{S3} = 145^\circ$, respectively. Also, the separation points over the second and the third domes move further downstream compared to the first dome for Re = 430,000.

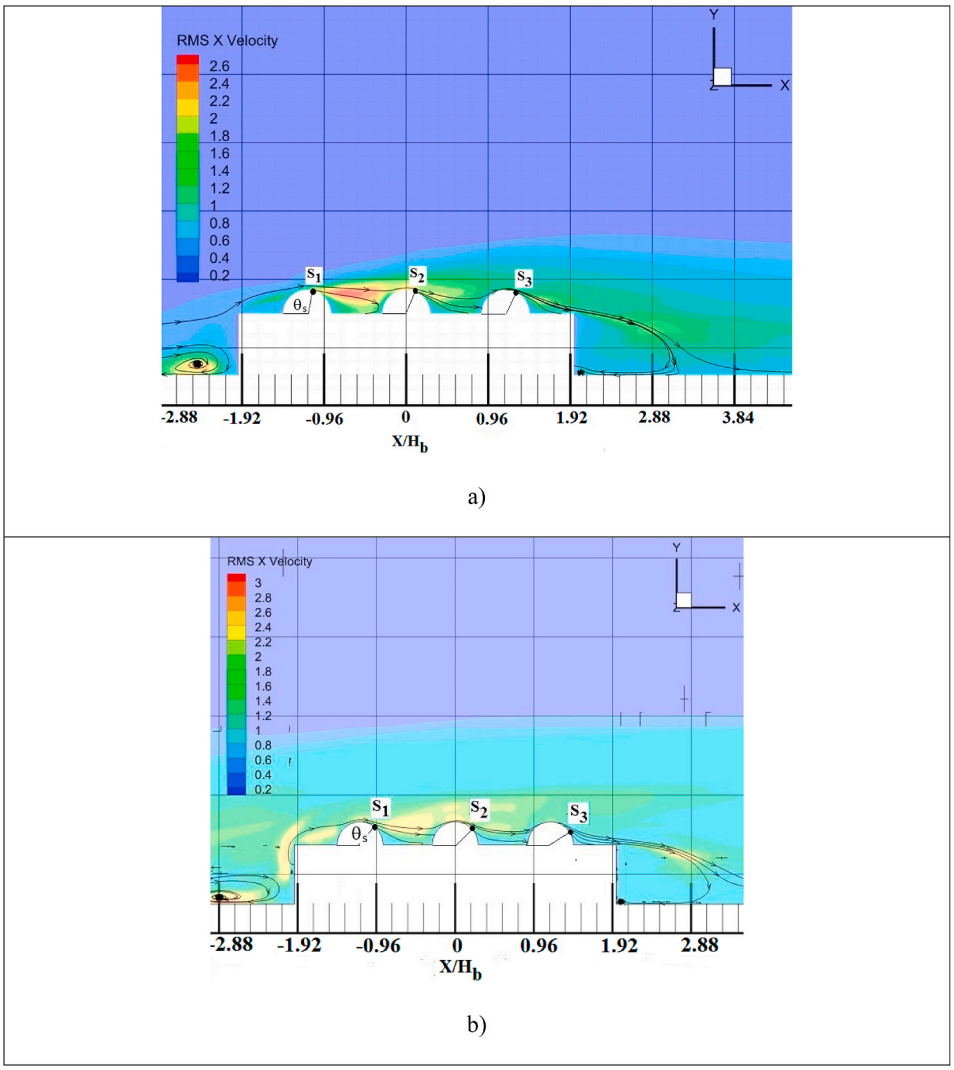

Fig. 14. Locations of separation points on symmetry plane over the domes overlaying the RMS streamwise velocity fluctuation contours. a) Re = 43,000. b) Re = 430,000.

4. Conclusions

A series of measurements and numerical simulations were performed, and the turbulent airflows around a model of building covered by an array of three domes were evaluated. The LES with the DKM SGS model and various grid resolutions were used, and the turbulent flow fields around the building model were studied. Mean velocity and RMS fluctuating velocity fields were evaluated and compared with the wind tunnel measurements. The complex vortical structures around the building, the pressure distributions over the domes, and the interference of domes in an array were also presented and discussed. It was shown that the velocity distributions predicted by the LES with fine grid were in good agreement with the measured wind tunnel data. This highlighted the importance of using proper grid resolution for the LES model to simulate the velocity field around a complex structure accurately. Another significant result is the locations of the maximum and minimum pressures over the domes in an array that were evaluated and reported in this study. Locations of peak suction are important for air-conditioned designers when the domes had an air vent to draw the air from the dome and enhance the natural ventilation and reduce the required air condition loads, especially in the hot arid climates. The maximum pressures and their locations on the domes are also important for the structural engineers to properly design the structure against the wind-induced load and increase its lifetime. Also, the knowledge gained from the current study for flow around a structure could be beneficial for the study of flow-structure interactions. Finally, the presented experimental data and numerical results may be used to validate other turbulence models.

Based on the presented results, the following conclusions are drawn:

1. The LES and RANS with the RNG k-ε model provide different results for the mean and fluctuating streamwise velocity profiles around the dome arrays. The RNG k-ε model does not correctly predict the mean velocity around the array of domes.
2. The LES with a fine grid was shown to reproduce the stream-wise velocity and RMS velocity distributions in the separated region downstream of the domes and behind the building model with reasonable accuracy. The LES with coarse and basic grids, however, do not adequately capture the reversed flow downstream of the third dome.
3. The results showed that the velocity fluctuations around the building were more sensitive to the grid resolution than the mean velocity profile. The LES with coarse and basic grids over-predicted the streamwise velocity fluctuations around the building model. The accurate prediction of velocity fluctuations is important for evaluating unsteady wind load on the structure, dispersion, and suspension of dust particles around the building, and design of the building ventilation system.

4. The maximum streamwise velocity fluctuations were observed over the roof upstream and downstream of the first dome. The LES with fine grid accurately predicted the maximum streamwise velocity fluctuations, while the RNG k-ε model under-predicted the velocity fluctuations.
5. The domes' peak suction pressure was seen over the first dome approximately at the dome apex for both Re = 43,000 and Re = 430,000. This suggests that the air vent at the first dome's apex is more effective in drawing air than the other domes in the array. Therefore, for enhancing the natural ventilation, it is recommended to use a larger vent in the first dome in the construction of dome arrays.
6. The maximum pressure over the domes occurred on the windward side of the third dome for both Re = 43,000 and Re = 430,000.
7. The separation point over the domes moved further downstream for the second and third domes due to increased velocity fluctuations over the roof for both Re = 43,000 and Re = 430,000.

It should be emphasized that the current study was concerned with the simulation of neutral boundary layer (NBL) flow, and the influence of thermal stratification was ignored. Previous studies, e.g., Willis and Deardorff [50], Fedorovich et al. [51], and Fedorovich and Kaiser [52], reported the wind tunnel experiment for simulation of convective boundary layers (CBLs). Recently, Marucci et al. [53] presented their results for a stable CBL over a very rough surface in a thermally-stratified wind tunnel. They found that with different levels of thermal stratification, the turbulent velocity profiles in the lower half of the boundary layer were substantially affected. In particular, Marucci et al. [53] reported a lower intensity of turbulence fluctuations for the CBLs compared to the NBL. With the lower level of incoming turbulence, previous studies of Savory and Toy [5,21] and Tavakol et al. [29] showed that the separation over a single dome/hemisphere occurs earlier. Therefore, it is expected that for the non-neutral boundary layer flow, the separation point at the midline over the domes in the array studied here moves to upstream. The earlier separations would change the pressure distribution and the reversed flow zones around the dome array.

Analyses of airflow for other configurations of dome arrays, the effect of thermal stratification, and particle dispersion and deposition around the building model are left for future studies.

Credit author statement

M.M. Tavakol: Conceptualization, Methodology, Software, Writing-Original draft preparation. M. Yaghoubi: Writing- Reviewing and Editing. G. Ahmadi: Writing- Reviewing and Editing.

Declaration of competing interest

The authors declare that they have no known competing financial interests or personal relationships that could have appeared to influence the work reported in this paper.

Acknowledgments

This research was financially supported by the Islamic Azad University, Shiraz Branch, Iran, through the project entitled "Numerical study of turbulent airflow and particle dispersion around a model of building with an array of domes."

References

[1] F.J. Maher, Wind loads on basic dome shapes, J. Struct. Div. 91 (3) (1965) 219–228.
[2] S. Taniguchi, H. Sakamoto, M. Kiya, M. Arie, Time-averaged aerodynamic forces acting on a hemisphere immersed in a turbulent boundary, J. Wind Eng. Ind. Aerod. 9 (3) (1982) 257–273.
[3] N. Toy, W.D. Moss, E. Savory, Wind tunnel studies on a dome in turbulent boundary layers, J. Wind Eng. Ind. Aerod. 11 (1–3) (1983) 201–212.
[4] Newman, B. G., Ganguli, U., & Shrivastava, S. C., Flow over spherical inflated buildings, J. Wind Eng. Ind. Aerod. 17 (3) (1984) 305–327.
[5] E. Savory, N. Toy, The flow regime in the turbulent near wake of a hemisphere, Exp. Fluid 4 (4) (1986) 181–188.
[6] T. Ogawa, M. Nakayama, S. Murayama, Y. Sasaki, Characteristics of wind pressures on basic structures with curved surfaces and their response in turbulent flow, J. Wind Eng. Ind. Aerod. 38 (2–3) (1991) 427–438.
[7] T.J. Taylor, Wind pressures on a hemispherical dome, J. Wind Eng. Ind. Aerod. 40 (2) (1992) 199–213.
[8] C.W. Letchford, P.P. Sarkar, Mean and fluctuating wind loads on rough and smooth parabolic domes, J. Wind Eng. Ind. Aerod. 88 (1) (2000) 101–117.
[9] C.M. Cheng, C.L. Fu, Characteristic of wind loads on a hemispherical dome in smooth flow and turbulent boundary layer flow, J. Wind Eng. Ind. Aerod. 98 (6–7) (2010) 328–344.
[10] T. Tamura, K. Kuwahara, M. Suzuki, Numerical study of wind pressures on a domed roof and near wake flows, J. Wind Eng. Ind. Aerod. 36 (1990) 1001–1010.
[11] R.N. Meroney, C.W. Letchford, P.P. Sarkar, Comparison of numerical and wind tunnel simulation of wind loads on smooth, rough and dual domes immersed in a boundary layer, Wind Struct. 5 (2002) 347–358.
[12] C.L. Fu, C.M. Cheng, Y.L. Lo, D.Q. Cheng, LES simulation of hemispherical dome's aerodynamic characteristics in smooth and turbulence boundary layer flows, J. Wind Eng. Ind. Aerod. 144 (2015) 53–61.
[13] M.N. Bahadori, F. Haghighat, Passive cooling in hot, arid regions in developing countries by employing domed roofs and reducing the temperature of internal surfaces, Build. Environ. 20 (2) (1985) 103–113.
[14] M.A. Yaghoubi, Air flow patterns around domed roof buildings, Renew. Energy 1 (3–4) (1991) 345–350.
[15] O.S. Asfour, M.B. Gadi, Using CFD to investigate ventilation characteristics of domes as wind-inducing devices in buildings, Int. J. Green Energy 4 (6) (2007) 571–588.
[16] A.K. Faghih, M.N. Bahadori, Experimental investigation of air flow over domed roofs, Iran. J. Sci. Technol. 33 (B3) (2009) 207–216.
[17] A.K. Faghih, M.N. Bahadori, Three dimensional numerical investigation of air flow over domed roofs, J. Wind Eng. Ind. Aerod. 98 (3) (2010) 161–168.
[18] M. Hadavand, M. Yaghoubi, Thermal behavior of curved roof buildings exposed to solar radiation and wind flow for various orientations, Appl. Energy 85 (8) (2008) 663–679.
[19] E. Sedighi, M. Yaghoubi, S.M. Mousavi, S. Siahpour, Thermal study of domed roofs in a traditional bazaar (the case of old Ganj-Alikhan bazaar in Kerman, Iran), Energy for Sustainable Development 39 (2017) 67–81.
[20] N. Kharoua, L. Khezzar, Large eddy simulation study of turbulent flow around smooth and rough domes, Proc. IME C J. Mech. Eng. Sci. 227 (12) (2013) 2686–2700.
[21] E. Savory, N. Toy, Hemisphere and hemisphere-cylinders in turbulent boundary layers, J. Wind Eng. Ind. Aerod. 23 (1986) 345–364.
[22] M.M. Tavakol, O. Abouali, M. Yaghoubi, Large eddy simulation of turbulent flow around a wall mounted hemisphere, Appl. Math. Model. 39 (13) (2015) 3596–3618.
[23] J.N. Wood, G. De Nayer, S. Schmidt, M. Breuer, Experimental investigation and large-eddy simulation of the turbulent flow past a smooth and rigid hemisphere, Flow, Turbul. Combust. 97 (1) (2016) 79–119.
[24] Y. Cao, T. Tamura, Large-eddy simulation study of Reynolds number effects on the flow around a wall-mounted hemisphere in a boundary layer, Phys. Fluids 32 (2) (2020), 025109.
[25] Y. Suzuki, M. Kiya, T. Sampo, Y. Naka, Pressure fluctuations on the surface of a hemisphere immersed in a thick turbulent boundary layer, J. Fluid Eng. 109 (2) (1987) 130–135.
[26] M.S. Acarlar, C.R. Smith, A study of hairpin vortices in a laminar boundary layer. Part 1. Hairpin vortices generated by a hemisphere protuberance, J. Fluid Mech. 175 (1987) 1–41.
[27] E. Savory, N. Toy, The separated shear layers associated with hemispherical bodies in turbulent boundary layers, J. Wind Eng. Ind. Aerod. 28 (1988) 291–300.
[28] M. Manhart, Vortex shedding from a hemisphere in a turbulent boundary layer, Theor. Comput. Fluid Dynam. 12 (1) (1998) 1–28.
[29] M.M. Tavakol, M. Yaghoubi, M.M. Motlagh, Air flow aerodynamic on a wall-mounted hemisphere for various turbulent boundary layers, Exp. Therm. Fluid Sci. 34 (5) (2010) 538–553.
[30] M. Fedrizzi, M. Giacobello, J. Soria, C. Atkinson, M. Jones, Experimental investigation of a hemisphere in a thin flat plate boundary layer, in: 18th Australasian Fluid Mechanics Conference, Launceston, Australia, 2012, December.
[31] A. Rahmatmand, M. Yaghoubi, E. Goshtasbi Rad, M.M. Tavakol, 3D experimental and numerical analysis of wind flow around domed-roof buildings with open and closed apertures, Building Simulation 7 (3) (2014) 305–319.
[32] J. Counihan, An improved method of simulating an atmospheric boundary layer in a wind tunnel, Atmos. Environ. 3 (2) (1969) 197–214.
[33] N.J. Cook, Determination of the model scale factor in wind-tunnel simulations of the adiabatic atmospheric boundary layer, J. Wind Eng. Ind. Aerod. 2 (4) (1978) 311–321.
[34] EDSU 85020, Characteristics of Atmospheric Turbulence Near the Ground: Strong Winds (Neutral Atmosphere), Engineering Sciences Data Unit, 1985, 85020.
[35] M.E. De Bortoli, B. Natalini, M.J. Paluch, M.B. Natalini, Part-depth wind tunnel simulations of the atmospheric boundary layer, J. Wind Eng. Ind. Aerod. 90 (4–5) (2002) 281–291.

[36] M.A. Ardekani, Hot-wire calibration using vortex shedding, Measurement 42 (5) (2009) 722–729.
[37] V. Yakhot, S.A. Orszag, S. Thangam, T.B. Gatski, C.G. Speziale, Development of turbulence models for shear flows by a double expansion technique, Phys. Fluid. A Fluid Dynam. 4 (7) (1992) 1510–1520.
[38] H.R. Haghighifard, M.M. Tavakol, G. Ahmadi, Numerical study of fluid flow and particle dispersion and deposition around two inline buildings, J. Wind Eng. Ind. Aerod. 179 (2018) 385–406.
[39] M. Germano, U. Piomelli, P. Moin, W.H. Cabot, A dynamic subgrid-scale eddy viscosity model, Phys. Fluid. Fluid Dynam. 3 (7) (1991) 1760–1765.
[40] W.W. Kim, S. Menon, An unsteady incompressible Navier–Stokes solver for large eddy simulation of turbulent flows, Int. J. Numer. Methods Fluid. 31 (6) (1999) 983–1017.
[41] D.K. Lilly, A proposed modification of the Germano subgrid-scale closure method, Phys. Fluid. Fluid Dynam. 4 (3) (1992) 633–635.
[42] B.R. White, Laboratory simulation of aeolian sand transport and physical modelling, Ann. Arid Zone 35 (3) (1996) 187–213.
[43] P.J. Richards, R.P. Hoxey, Appropriate boundary conditions for computational wind engineering models using the k-ε turbulence model, in: Computational Wind Engineering, vol. 1, Elsevier, 1993, pp. 145–153.
[44] Y. Tominaga, A. Mochida, R. Yoshie, H. Kataoka, T. Nozu, M. Yoshikawa, T. Shirasawa, AIJ guidelines for practical applications of CFD to pedestrian wind environment around buildings, J. Wind Eng. Ind. Aerod. 96 (10–11) (2008) 1749–1761.
[45] E. Sergent, Vers une methode de couplage entre la simulation des grandes echelles et les mod eles statistiques (in French), PhD thesis at Ecole doctoral MEGA, L'Ecole Centrale de Lyon, France, 2002.
[46] T. van Hooff, B. Blocken, Y. Tominaga, On the accuracy of CFD simulations of cross-ventilation flows for a generic isolated building: comparison of RANS, LES and experiments, Build. Environ. 114 (2017) 148–165.
[47] M. Schatzmann, H. Olesen, J. Franke (Eds.), COST 732 Model Evaluation Case Studies: Approach and Results, COST Office Brussels, Belgium, 2010.
[48] Y. Tominaga, T. Stathopoulos, Steady and unsteady RANS simulations of pollutant dispersion around isolated cubical buildings: effect of large-scale fluctuations on the concentration field, J. Wind Eng. Ind. Aerod. 165 (2017) 23–33.
[49] J.C.R. Hunt, A.A. Wray, P. Moin, Eddies, stream and convergence zones in turbulent flows, Report CTR-S88, in: Proceeding of the 1998 Summer Program, Stanford N.A.S.A Center for Turbulence Research, Stanford, CA, 1988.
[50] G.E. Willis, J.W. Deardorff, A laboratory model of the unstable planetary boundary layer, J. Atmos. Sci. 31 (5) (1974) 1297–1307.
[51] E. Fedorovich, Dispersion of passive tracer in the atmospheric convective boundary layer with wind shears: a review of laboratory and numerical model studies, Meteorol. Atmos. Phys. 87 (1–3) (2004) 3–21.
[52] E. Fedorovich, R. Kaiser, Wind tunnel model study of turbulence regime in the atmospheric convective boundary layer, in: Buoyant Convection in Geophysical Flows (Pp. 327-370). Springer, Dordrecht, 1998.
[53] D. Marucci, M. Carpentieri, P. Hayden, On the simulation of thick non-neutral boundary layers for urban studies in a wind tunnel, Int. J. Heat Fluid Flow 72 (2018) 37–51.